Supporting Information for "The importance of ice sheet growth and retreat on magmatism and mantle CO$_2$ flux"

John J. Armitage[1], David J. Ferguson[2], Kenni D. Petersen[3], and Timothy

T. Creyts[4]

[1]Dynamique des Fluides Géologiques, Institut de Physique du Globe de Paris, Paris, France

[2]School of Earth and Environment, University of Leeds, Leeds, U.K.

[3]Department of Geoscience, University of Aarhus, Aarhus, Denmark

[4]Lamont-Doherty Earth Observatory, Columbia University, U.S.A

Contents of this file

1. Text S1 to S3

2. Figures S1 to S4

Additional Supporting Information (Files uploaded separately)

1. Table S1

2. Data Set S1

———————

April 5, 2019, 1:53pm

Introduction We develop a model of lithosphere flexure due to the glaciation and deglaciation that is coupled to melting within the asthenosphere and the subsequent transport of that melt to the surface. In order to drive the model we also must estimate past Icelandic ice sheet thickness (see Text S1 below). What follows is a description of these two models.

Text S1.

Generating an Ice sheet History

Our goal is to create realizations of ice loading over the Iceland rift zone. The ice volume history of Iceland through the entire last glacial period is fragmentary, and poorly constrained prior to the Last Glacial Maximum (26-110 ka) (Geirsdóttir, 2011). This lack of information is a result of the growth of the ice sheet to the LGM (∼19-26.5 ka) (Clark et al., 2009; Geirsdóttir, 2011), because it reworks prior deposits and remobilizes sediments, obscuring the earlier record (Andrews, 2008). Additionally, we are mainly interested in the loading history and less concerned with the extent, glacial features, or ice rafted debris, that are specific to the extent and configuration of the Icelandic Ice Sheet. We therefore only require a realization from which to run the melting model. Hence we believe simplified ice sheet history is sufficient to understand the magmatism in Iceland.

We develop a simple method of reconstructing the volume using published ice sheet model results. We use the results of Patton, Hubbard, Bradwell, and Schomackere (2017) to identify the ice thickness over the rift zone. Their model results are designed to understand the configuration of the ice sheet during the deglaciation. This time period is also the best constrained in terms of the sea level history (Andersen et al., 2004; Spratt &

Lisiecki, 2016) and deglacial climate (Lambeck & Chappel, 2001). Recognizing that the Patton et al. (2017) model is driven by the NGRIP climate record (Lambeck & Chappel, 2001) and also that the volume of ice sheets is also contained in sea level histories (Spratt & Lisiecki, 2016), we use these to constrain ice sheet history prior to the LGM.

We create rift zone loading histories that extend back through the last glacial to the previous interglacial period. We perform a parametric regression on the rift ice load, the NGRIP $\delta^{18}O$ record, and the deglacial sea level record through the deglaciation. We then use the coefficients of the deglacial history to extend the ice sheet load back in time using published sea level records (Peltier, 2004; Pico, Creveling, & Mitrvica, 2017).

We regress the ice sheet results against the ice core $\delta^{18}O$ (Lambeck & Chappel, 2001) and the relative sea level curve (Spratt & Lisiecki, 2016):

$$v_{ind} = a_1 \delta_{NGRIP} + a_2 \Delta \zeta_{esl} + c \tag{1}$$

We seek an index for the volume of the Icelandic Ice Sheet v_{ind} by solving for the coefficients a_1 and a_2, as well as the offset c, where δ_{NGRIP} is the ice core oxygen isotope record and $\Delta \zeta_{esl}$ is the relative sea level height. We use the results of Patton et al. (2017) from 10 ka to 23.5 ka so that $a_1 = -21.94$, $a_2 = -4.993$. Figure S1 shows how each of the input time series yields the scaled time series. We then apply these coefficients to the remainder of the NGRIP and sea level histories to get the loading from 120,000 years to the present (Figure S2). Because sea level is not well-constrained through the last glacial period, we utilize three different sea level curves to produce the relative ice sheet volume (Figure S2). We then scale the ice sheet histories to give a maximum ice sheet thickness of 1800 m. We force the melting model with the two ice sheet histories, the M1 model based on the sea

April 5, 2019, 1:53pm

level curve ICE-5G (Peltier, 2004) and the model M2 based on the sea level curve of Pico et al. (2017).

Text S2.

Numerical Melting Model Description and Methods

We solve for the conservation of energy and the vertical percolation of melt within a one-dimensional vertical column. We define a average velocity of the solid and liquid phases (Scott, 1992),

$$\bar{v} = (1 - \phi)v_s + \phi v_l, \tag{2}$$

where ϕ is porosity, v_s is the solid mantle velocity, v_l is the melt velocity. All model parameters are listed in Table S1. The change in surface load is assumed to impact the average velocity. We calculate the displacement due to a ice sheet where the change in surface displacement, w_0, with time is given by (Sleep & Snell, 1976),

$$N\frac{\partial^4}{\partial x^4}\left(\frac{\partial w_0}{\partial t}\right) = \frac{P_{ice}}{\tau_e}, \tag{3}$$

where N is the elastic flexural rigidity, P_{ice} is the load due to the ice sheet, and τ_e is the viscoelastic decay time. The elastic flexural rigidity is given by,

$$N = \frac{ET_e}{12(1 - \mu^2)}, \tag{4}$$

where E is Young's modulus, T_e is the effective elastic thickness, and μ is Poisson's ratio. The viscoelastic decay time is defined as (Sleep & Snell, 1976),

$$\tau_e = \frac{3\eta_s}{E}, \tag{5}$$

where η_s is the viscosity of the lithosphere. Equation 3 is solved using a simple finite element model with linear weighting functions, to solve for w_0 as a function of time due to

April 5, 2019, 1:53pm

the change in surface load. The vertical velocity of the mantle below is then updated by the rate of change in displacement due to the surface load, assuming that the displacement decays with depth as a function of the wavelength (width), λ, of the ice load (England, Houseman, & Sonder, 1985),

$$w = w_0 exp\left(-\sqrt{3}\pi\frac{z}{\lambda}\right). \tag{6}$$

Therefore the vertical velocity is given by,

$$\bar{v} = u + \frac{\partial w}{\partial t}, \tag{7}$$

where u is the constant upwelling rate.

The model is then either run as a single upwelling column with a fixed upwelling rate (1D) or we use the steady state solution to the corner flow of mantle hitting a horizontal plain to get create a 2D flow field from which to extract the vertical upwelling rate (Silbeck, 1975). In the 1D version the displacement at the centre of the model, $\partial w/\partial t$, is used to perturb the vertical velocity, while in the 2D version we take take a width of displacement from 0 to 80 km from the centre of extension, and assume melt travels vertically upwards in 1D columns. The displacement at each point from 0 to 80 km is used to perturb the vertical velocity from the corner flow solution.

To calculate the vertical flow of melt as function of variations in the decompression rate, the conservation of energy is given by,

$$mL + \frac{\partial T}{\partial t} + \bar{v}\frac{\partial T}{\partial z} - \kappa\frac{\partial^2 T}{\partial z^2} = 0, \tag{8}$$

where m is the melt production rate, L is the latent heat of fusion, T is temperature, and κ is the thermal diffusion coefficient. The latent heat is given by, $L = T\Delta S/C_p$, where

ΔS is the entropy change due to melting and C_p is the heat capacity. The conservation of mass for the liquid phase is given by,

$$\frac{\partial \phi}{\partial t} + \frac{\partial}{\partial z}(\phi v_l) = m. \tag{9}$$

To relate the solid velocity to the liquid velocity we turn to Darcy's law,

$$\phi(v_l - v_s) = \frac{k_0 \phi^n}{\eta_l}\left(\Delta \rho g + \frac{\partial P}{\partial z}\right), \tag{10}$$

where k_0 is the permeability coefficient, n is the exponent on the assumed power law relation between permeability and porosity, $\Delta \rho$ is the density difference between melt and the solid mantle, g is gravity, and P is the pore pressure. We simplify equation 10 by assuming that the compaction length scale is very small, the zero-compaction length approximation (Ribe, 1985). This means that Darcy's law becomes,

$$\phi(v_l - v_s) = \frac{k_0 \phi^n}{\eta_l}\Delta \rho g. \tag{11}$$

Furthermore, we substitute v_s with the average velocity (equation 2) to get,

$$(v_l - \bar{v}) = (1 - \phi)\frac{k_0 \phi^{n-1}}{\eta_l}\Delta \rho g. \tag{12}$$

This form of Darcy's law allows us to substitute for v_l within the conservation of the liquid phase. Based on laboratory experiments, where permeability is found to be related to porosity to the power of $n = 2.6 \pm 0.2$ (Miller, Zhu, Montési, & Gaetani, 2014), we assume $n = 3$, to give,

$$\frac{\partial \phi}{\partial t} + \bar{v}\frac{\partial \phi}{\partial z} + \frac{3 k_0 \Delta \rho g}{\eta_l}\phi^2\left(1 - \frac{4}{3}\phi\right)\frac{\partial \phi}{\partial z} = m. \tag{13}$$

Here we also assume that $\partial \bar{v}/\partial z \sim 0$.

Equations 8 and 13 are coupled by the melt production rate. We calculate the melting rate from the temperature difference above the solidus. The solidus is a function of water

content, depletion, temperature and pressure. In the energy balance we have ignored the loss of heat as the mantle decompresses, but the adiabatic gradient needs to be accounted for within the thermodynamic balance for the melting equations. Assuming the mantle is dehydrated it is calculated as,

$$T_{Sdry} = T_{S0} + \frac{\partial T_S}{\partial F}|_P F + \left(\frac{\partial T_S}{\partial P}|_F + \frac{\alpha T_0}{\rho C_p} \right) P, \tag{14}$$

where $\partial T_S/\partial F|_P$ is the solidus depletion gradient, F is depletion, $\partial T_S/\partial P|_F$ is the solidus pressure gradient, α is the coefficient of thermal expansion, C_p is the heat capacity, and P is pressure. We assume a mantle source that has 60% primitive mantle and 40% MORB (Shorttle & Maclennan, 2011), and therefore is depleted relative to fertile mantle. We therefore assume a slightly higher solidus depletion gradient of $800\,°C$ (Armitage, Collier, Minshull, & Henstock, 2011; Wasylenki, Baker, Kent, & Stopler, 2003). This means that at steady state our models generate a depletion of roughly 10%.

The solidus is assumed to deepen in the presence of water,

$$T_{Swet} = T_{Sdry} + K \left(D_{H_2O} C_{H_2O} \right)^\gamma, \tag{15}$$

where the coefficients K and γ are from the parameterisation of Katz, Spiegelman, and Langmuir (2003) (their equation 16), D_{H_2O} is the partition coefficient for water, and C_{H_2O} is the concentration of water within the solid mantle. Therefore the melt productivity is given by,

$$m = \frac{\Delta T}{L + \frac{\partial T_S}{\partial F}|_P + \frac{\partial T_S}{\partial F}|_{H_2O}}, \tag{16}$$

where $\Delta T = T - T_{Swet}$ is the temperature difference between the mantle and the wet solidus, and $\partial T_S/\partial F|_{H_2O}$ is the solidus depletion gradient during the melting of a hydrated

mantle. This is calculated using the chain rule,

$$\frac{\partial T_S}{\partial F}\Big|_{H_2O} = \frac{\partial T_S}{\partial C_{H_2O}}\frac{\partial C_{H_2O}}{\partial F}. \tag{17}$$

The change in water composition as a function of depletion is calculated assuming a mass balance between the partitioning of water between the solid and melt phase,

$$\frac{\partial C_{H_2O}}{\partial F} = -C_{H_2O}\frac{1}{D_{H_2O}}(1-F)^{\frac{1}{D_{H_2O}}-2} \tag{18}$$

and the gradient in solidus with water composition is from equation 15,

$$\frac{\partial T_S}{\partial C_{H_2O}} = \gamma K \left(D_{H_2O}C_{H_2O}\right)^{\gamma-1} \tag{19}$$

The calculation of melt production described in equations 14 to 19 can be unstable for small time steps as temperature is a function of the melt production and the melt production is a function of the temperature. The mantle composition also feeds back into the solidus and hence melt production. If the jump in temperature due to the movement of the solid mantle between time steps is too large, the model can become unstable. To improve stability we therefore implemented a simple Runga Kutta scheme to solve equations 14 to 19 once the temperature solution was found.

To track the composition of the melt we assume disequilibrium melting, where the conservation of the solid composition, C_s, is given as (Spiegelman, 1996),

$$\frac{\partial C_s}{\partial t} + v_s\frac{\partial C_s}{\partial z} = \left(\frac{1}{D}-1\right)\frac{C_s m}{1-\phi}, \tag{20}$$

and the melt composition, C_l, can be written as follows (Spiegelman, 1996),

$$\frac{\partial C_l}{\partial t} + v_l\frac{\partial C_f}{\partial z} = \left(\frac{C_S}{D}-C_l\right)\frac{m}{\phi}. \tag{21}$$

The melt composition is calculated from the solid composition and knowledge of the partition coefficient D. The partition coefficient is a function of the mineral phase stability

(McKenzie & O'Nions, 1991),

$$D = f_{ol}\mathcal{D}_{ol \to melt} + f_{opx}\mathcal{D}_{opx \to melt} + f_{cpx}\mathcal{D}_{cpx \to melt} + f_X \mathcal{D}_{X \to melt} \qquad (22)$$

where f is the proportion of each mineral within plagiolcase, spinel, and garnet peridotite, D_{ol}, etc, are the partition coefficients for Nb and carbon for each phase into melt, and X represents plagioclase, spinel and garnet, respectively. The values for f are taken from Gibson and Geist (2010). For the trace element Nb we use the partition coefficients cited in Gurenko and Chaussidon (1995), and for carbon we use the partition coefficients of Rosenthal, Hauri, and Hirschmann (2015). As previously mentioned, the initial mantle composition of Nb is assumed to be that of 60 % primitive mantle and 40 % MORB (Shorttle & Maclennan, 2011). The water composition of the solid mantle is advected using equation 20, assuming a partition coefficient of 0.01 for all phases.

To convert the predicted concentration of carbon to a flux of CO_2 we assume that the flux of carbon is given by,

$$\Psi_{CO_2} = 3.69 C_C A \rho_l \phi^{surface} (v_l - v_s)_{surface} \qquad (23)$$

where the factor 3.67 accounts for the conversion of carbon to CO_2, C_C is the carbon concentration in the melt at $\phi_{surface}$, the upper boundary of the model, and A is the surface area of magmatism, which is assumed to be $30{,}000\,\mathrm{km}^2$.

We first solve equations 8 and 13, decomposing the diffusion and advection components and using a standard second order accurate explicit finite difference scheme for the diffusion and a flux conservative total variance diminishing (TVD) scheme for the advection term. Once we have solved for porosity and temperature, we calculate the melt and solid velocity using equation 2, and update the solid and melt compositions (equations 20 and

21) using the the same TVD scheme. The codes, written in MATLAB, are available at

https://bitbucket.com/johnjarmitage/melt1d-icesheet/.

Model Evolution due to Step Changes in Ice Sheet Thickness

We perturb the model with a periodic step function of glaciation and deglaciation that has a periodicity of 40 ka (Figure S3a). The peak in eruption rate is sensitive to the permeability (Figure S3b). The peak occurs sooner and with greater intensity if the permeability coefficient is high ($10^{-5}\,m^2$; Figure S3b). This is because the rate of melt percolation is much more rapid if the melt permeability is high (Burley & Katz, 2015). In contrast, for a lower permeability coefficient, $10^{-7}\,m^2$, the peak in melt production is diluted by the slower melt transport, and the signal of increased melt production reaches the surface with a delay of a few thousand years (Figure S3b). Glaciation acts to gradually shut down melt generation, as the signal of surface displacement travels down the 1-D model (Figure S3b). Carbon fluxes mirror the trend in melt eruption rate (Figure S3c), with sharp peaks upon deglaciation due to the increased flux of melt. We do not observe a significant delay between the CO_2 flux and eruption rate (Burley & Katz, 2015), as we find that carbon partitions into the melt not only at the on-set of melt production but throughout the deep zone of partial melting. If the permeability coefficient is high, $10^{-5}\,m^2$, there is a broad bulge in CO_2 flux that arrives after the peak. This secondary pulse is due to the arrival of deep carbon rich melts percolating upwards as the lower regions of the zone of partial melting recover.

Steady state melt thickness The thickness of melt delivered to the model upper surface can be calculated from the 2D version of the code, where we assume a corner flow for the

mantle and model melt percolation as a set of vertical columns:

$$h_{melt} = \frac{1}{v_{spread}} \int (v_l(x) - v_s(x))_{surface} \, \phi_{surface}(x) dx \qquad (24)$$

where v_{spread} is the half spreading rate for the corner flow solution. The steady state melt thickness defined by this equation gives a steady state thickness of $20\,\text{km}$ (Figure S4).

Data Set S1.

The observed Nb compositions come from Eason, Sinton, Gronvöld, and Kurz (2015); Gee, Taylor, Thirwall, and Murton (1998); Sinton, Grönvold, and Saemundsson (2005) and are in the supplementary Data Set S1. Observed Nb concentrations were corrected for the effects of crystal fractionation/accumulation assuming a parental melt with MgO of $\sim 14\,\text{wt}\,\%$ and perfect incompatibility of Nb during crystallisation. They are subsequently binned at $2.5\,\text{kyr}$ intervals from 0 to $17.5\,\text{ka}$ and subsequently binned at 5 kyr intervals. The mean is plotted with the error bars representing one standard deviation (Figures 5 and 4 in the main text).

References

Andersen, K. K., Azuma, N., Barnola, J. M., Bigler, M., Biscaye, P., Caillon, N., ... White, J. W. C. (2004). High-resolution record of northern hemisphere climate extending into the last interglacial period. *Nature*, *431*, 174-151. (doi: 10.1038/nature02805)

Andrews, J. T. (2008). The role of the Iceland Ice Sheet in the North Atlantic during the late Quaternary: a review and evidence from Denmark Strait. *Journal of Quaternary Science*, *23*, 3-20. (doi: 10.1002/jqs.1142)

Armitage, J. J., Collier, J. S., Minshull, T. A., & Henstock, T. J. (2011). Thin oceanic

crust and flood basalts: India-Seychelles breakup. *Geochemistry Geophysics Geosystems*, *12*(Q0AB07). (doi:10.1029/2010GC003316)

Burley, J. M. A., & Katz, R. F. (2015). Variations in mid-ocean ridge CO_2 emissions driven by glacial cycles. *Earth and Planetary Science Letters*, *426*, 246-258. (doi: 10.1016/j.epsl.2015.06.031)

Clark, P. U., Dyle, A. S., Shakun, J. D., Carlson, A. E., Clark, J., Wohlfarth, B., ... McCabe, A. M. (2009). The last glacial maximum. *Science*, *325*, 710. (doi: 10.1126/science.1172873)

Eason, D. E., Sinton, J. M., Gronvöld, K., & Kurz, M. D. (2015). Effects of deglaciation on the petrology and eruptive history of the Western Volcanic Zone, Iceland. *Bulletin of Volcanology*, *77*(47). (doi: 10.1007/s00445-015-0916-0)

England, P., Houseman, G., & Sonder, L. (1985). Length scales for continental deformation in convergent, divergent, and strike-slip environments: analytical and approximate solutions for a thin viscous sheet model. *Journal of Geophysical Research*, *90*(B5), 355103557.

Gee, M. A. M., Taylor, R. N., Thirwall, M., & Murton, B. J. (1998). Glacioisostacy controls chemical and isotopic characteristics of tholeiites from the Reykjanes Peninsula, SW Iceland. *Earth and Planetary Science Letters*, *164*, 1-5.

Geirsdóttir, A. (2011). Pliocene and pleistocene glaciations of iceland: a brief overview of the glacial history. In J. Ehlers, P. L. Gibbard, & P. Hughes (Eds.), *Quaternary glaciations - extent and chronology, a closer look* (Vol. 15, p. 199-210). Elsevier. (doi: 10.1016/B978-0-444-53447-7.00016-7)

Gibson, S. A., & Geist, D. (2010). Geochemical and geophysical estimates of lithospheric thickness variation beneath galápagos. *Earth and Planetary Science Letters*, *300*, 275-286. (doi: 10.1016/j.epsl.2010.10.002)

Gurenko, A. A., & Chaussidon, M. (1995). Enriched and depleted primitive melts included in olivine from icelandic tholeiites: Origin by continuous melting of a single mantle column. *Geochimica et Cosmochimica Acta*, *59*, 2905-2917.

Katz, R. F., Spiegelman, M., & Langmuir, C. H. (2003). A new parameterization of hydrous mantle melting. *Geochemistry Geophysics Geosystems*, *4*, 1073. (doi: 10.1029/2002GC000433)

Lambeck, K., & Chappel, J. (2001). Sea level change through the last glacial cycles. *Science*, *292*, 679-686. (doi: 10.1126/science.1059549)

Lambeck, K., Rouby, H., Purcell, A., Sun, Y., & Sambridge, M. (2014). Sea level and global ice volumes from the Last Glacial Maximum to the Holocene. *Proceedings of the National Academy of Sciences*, *111*, 15296-15303. (doi: 10.1073/pnas.141176211)

McKenzie, D., & O'Nions, R. K. (1991). Partial melt distribution from inversion of rare earth element concentrations. *Journal of Petrology*, *32*, 1021-1091.

Miller, K. J., Zhu, W., Montési, L. G. J., & Gaetani, G. A. (2014). Experimental quantification of permeability of partially molten mantle rock. *Earth and Planetary Science Letters*, *388*, 273-282. (doi: 10.1016/j.epsl.2013.12.003)

Patton, H., Hubbard, A., Bradwell, T., & Schomackere, A. (2017). The configuration, sensitivity and rapid retreat of the Late Weichselian Icelandic ice sheet. *Earth-Science Reviews*, *166*, 223-245. (doi: 10.1016/j.earscirev.2017.02.001)

Peltier, W. R. (2004). Global glacial isostacy and the surface of the ice-age Earth: The ICE-5G (VM2) model and grace. *Annual Reviews of Earth and Planetary Science*, *32*, 111-149. (2004)

Pico, T., Creveling, J. R., & Mitrvica, J. X. (2017). Sea-level records from the U.S. mid-Atlantic constrain Laurentide Ice Sheet extent during Marine Isotope Stage 3. *Nature Communications*, *8*(15621). (doi: 10.1038/ncomms15612)

Ribe, N. M. (1985). The generation and composition of partial melts in the earth's mantle. *Earth and Planetary Science Letters*, *73*, 361-376.

Rosenthal, A., Hauri, E. H., & Hirschmann, M. M. (2015). Experimental determination of C, F, and H partitioning between mantle minerals and carbonated basalt, CO_2/Ba and CO_2/Nb systematics of partial melting, and the CO_2 contents of basaltic source regions. *Earth and Planetary Science Letters*, *415*, 77-87. (doi: 10.1016/j.epsl.2014.11.044)

Scott, D. R. (1992). Small-scale convection and mantle melting beneath mid-ocean ridges. In J. Phipps Morgan, D. K. Blackman, & J. M. Sinton (Eds.), *Mantle flow and melt generation at mid-ocean ridges* (Vol. Geophysical Monograph 71, p. 327-352). American Geophysical Union.

Shorttle, O., & Maclennan, J. (2011). Compositional trends of icelandic basalts: Implications for short-length scale lithological heterogeneity in mantle plumes. *Geochemistry Geophysics Geosystems*, *12*, Q11008. (doi: 10.1029/2011GC003748)

Silbeck, J. N. (1975). On the fluid dynamics of ridge crests. In *Notes on the 1975 summer study program in geophysical fluid dynamics at the woods hole oceanographic*

institution, (Vol. 2, p. 113-122).

Sinton, J., Grönvold, K., & Saemundsson, K. (2005). Postglacial eruptive history of the
Western Volcanic Zone, Iceland. *Geochemistry Geophysics Geosystems*, *6* (Q12006).
(doi: 10.1029/2005GC001021)

Sleep, N. H., & Snell, N. S. (1976). Thermal contraction and flexure of mid-continent and
Atlantic marginal basins. *Geophysical Journal of the Royal Astronomical Society*, *45*,
125-154.

Spiegelman, M. (1996). Geochemical consequences of melt transport in 2-D: The sensi-
tivity of trace elements to mantle dynamics. *Earth and Planetary Science Letters*,
139, 115-132.

Spratt, R. M., & Lisiecki, L. E. (2016). A late Pleistocene sea level stack. *Climate of the
Past*, *12*, 1079-1092. (doi: 10.5194/cp-12-1079-2016)

Wasylenki, L. E., Baker, M. B., Kent, A. J. R., & Stopler, E. M. (2003). Near-solidus
melting of the shallow upper mantle: partial melting experiments on depleted peri-
dotite. *Journal of Petrology*, *44*, 116-1191.
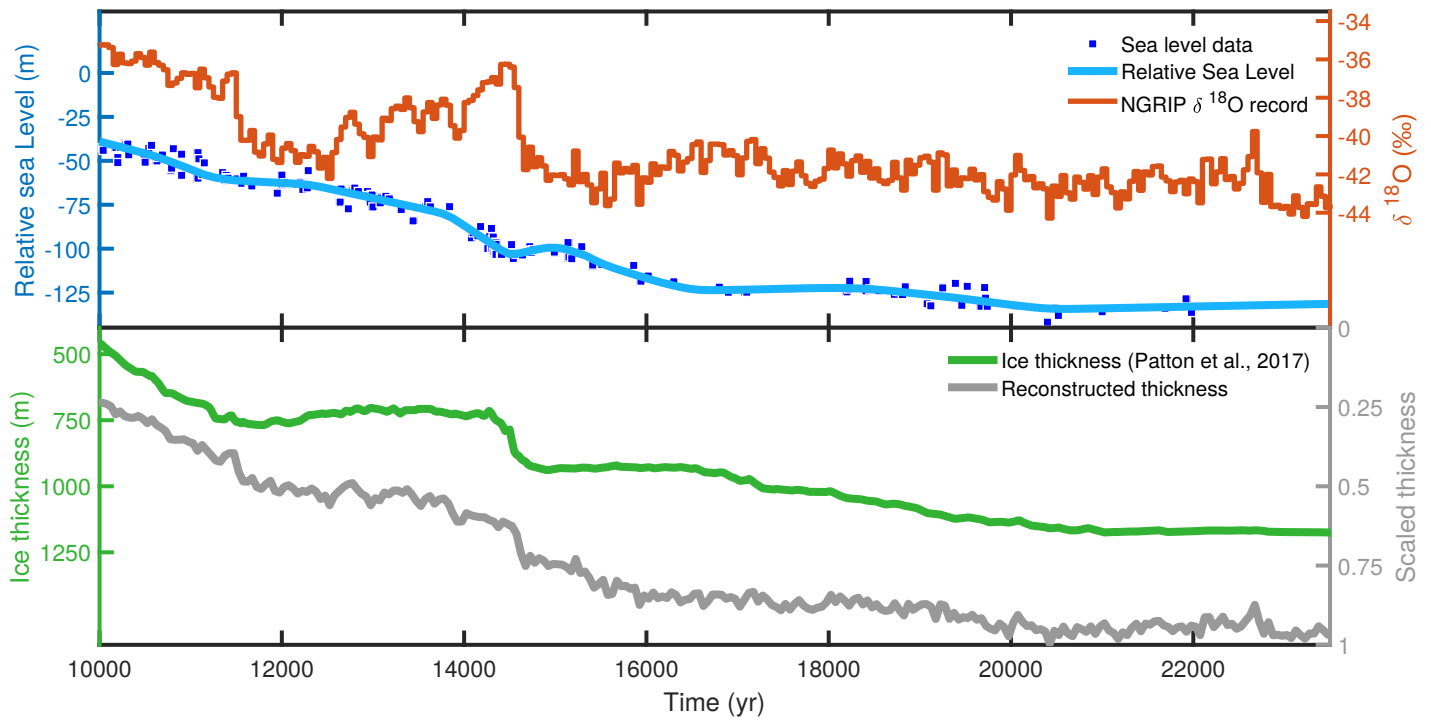
Figure S1. We use the NGRIP δ^{18}O, relative sea level history (Spratt & Lisiecki, 2016), and ice thickness results (Lambeck et al., 2014) to create a scaled thickness of the Icelandic Ice Sheet through the deglaciation. Our resultant history tends to preserve some high frequency characteristics of the δ^{18}O record but mutes larger changes such as decrease in ice thickness at the start of the Bolling-Allerod ($\sim$14.7 ka).

Table S1. List of model parameters.
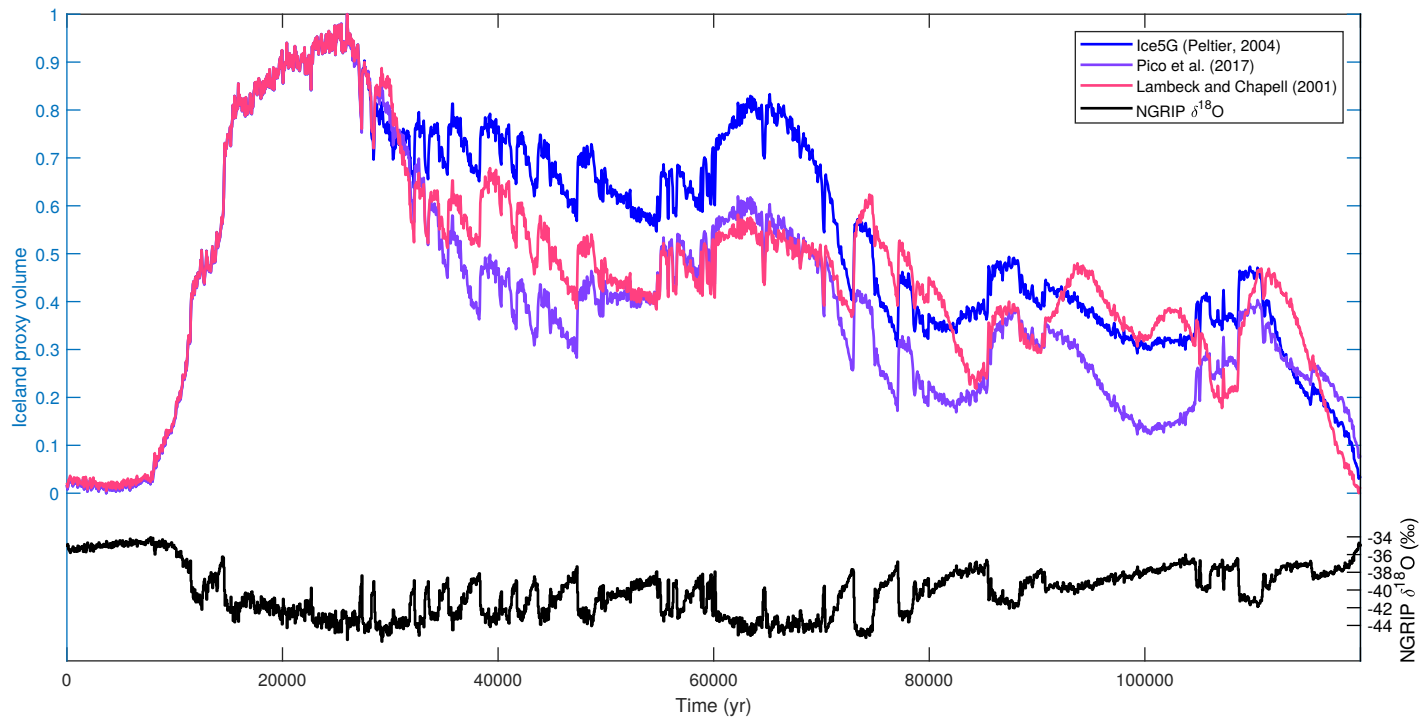
Figure S2. Reconstructed ice volumes for 120,000 years to present. Here, we use the differing relative sea level reconstructions (Lambeck & Chappel, 2001; Peltier, 2004; Pico et al., 2017) to infer the relative volume of ice in Iceland. The curves match thought the regression period of 10000-23500 years.
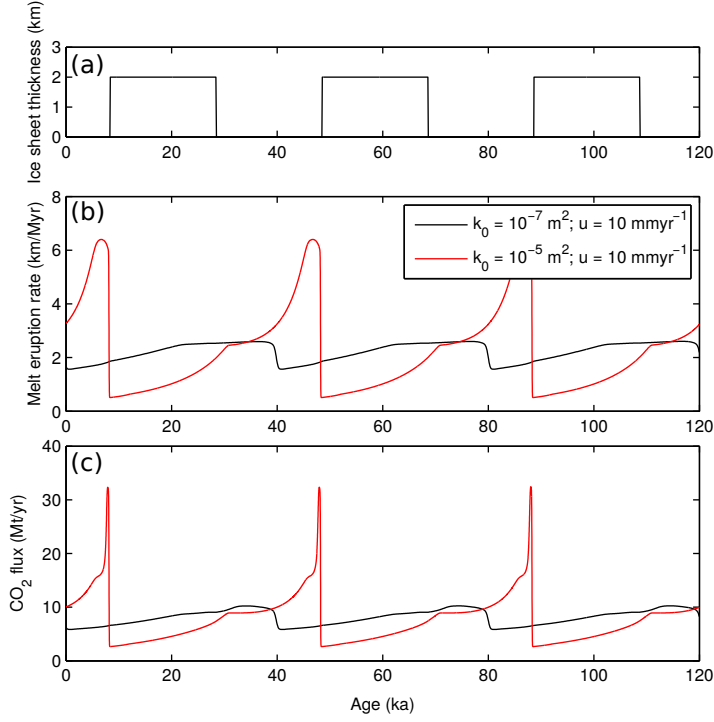
Figure S3. Model response to a repeated step change ice sheet thickness. (A) Periodic change in ice sheet thickness assuming a width, λ, of $200\,\mathrm{km}$. (B) Model response in terms of eruption rate. Here the model elastic thickness is $10\,\mathrm{km}$, the viscosity is $10^{21}\,\mathrm{Pa\,s}$, the upwelling rate is $10\,\mathrm{mm\,yr}^{-1}$, and the mantle temperature is $1450\,^{\circ}\mathrm{C}$. The black line is for a permeability coefficient of $10^{-7}\,\mathrm{m}^2$, and the red line is for a permeability coefficient of $10^{-5}\,\mathrm{m}^2$. (C) Model response in terms of CO_2 flux.
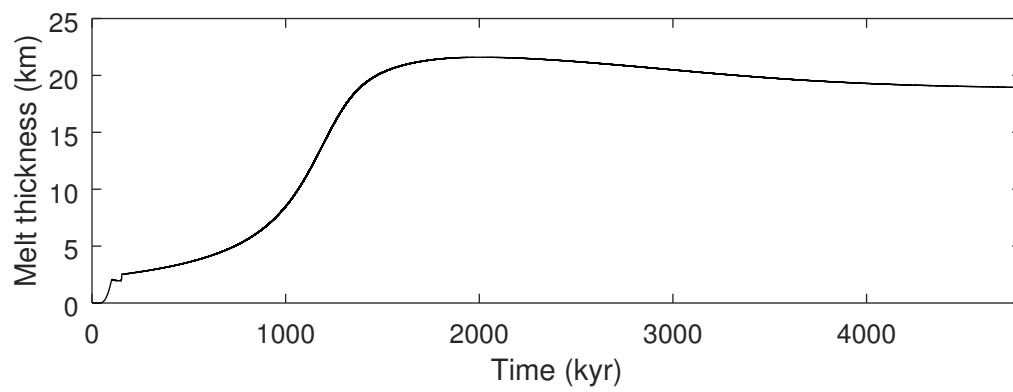
Figure S4. Prediction of melt thickness assuming a mantle temperature of $1450\,°C$ and a half spreading rate of $10\,\mathrm{mm\,yr^{-1}}$.